ROYAL SOCIETY
OF CHEMISTRY

PAPER

Modelling of formic acid production using solventless trialkylamine reduction strategies†

A. W. N. de Leeuw den Bouter, [ab] A. Miquelot,[b] L. Brito, [c] P. Olivier[b] and J. van der Schaaf [*a]

Solventless fed-batch experiments at elevated pressures were performed to gain insights into the performance of triethylamine as an extraction base during the direct hydrogenation of CO_2 to formic acid. No formic acid was observed in the bulk liquid after several hours of reaction using an Au/TiO_2 catalyst. Analysis on the spent catalyst revealed significant formic acid build-up within the catalyst pores. A fundamental, continuum model based on Cahn–Hilliard spinodal decomposition was developed and validated to study the influence of the biphasic nature of formic acid – trialkylamine structures during reaction at pore level. The biphasic nature of the tertiary alkylamine – formic acid system was found to have significant implications for the reaction performance of the proposed system, demonstrating the requirement of additional solvents besides tertiary amines to ensure solubility of the complete system.

Introduction

The last decades have witnessed an unprecedented increase in CO_2 concentrations in the atmosphere due to an exponential growth of the global population, resulting in an increase in fossil fuel consumption.[1,2] These anthropogenic carbon emissions have been linked to negative environmental impact,[1] such as global temperature increases, the disappearance of the glaciers and the acidification of the oceans.[1,3,4] For this reason, there is significant political and scientific interest in the prevention and mitigation of CO_2 emissions.[5,6]

One possibility often considered viable for effective CO_2 emission mitigation is the concept of carbon capture and utilization (CCU), where the carbon dioxide is utilized for the production of higher-value chemicals and fuels.[2,3,7] Herein, CO_2 is employed as a C1 source as a wide range of products such as formic acid, methanol and methane.[1,8,9] Formic acid (FA) is an interesting product due to widespread application within the pharmaceutical, agricultural and textile industries[1,3,10] resulting in a global market of 800 kton per year.[7,11]

The demand is expected to increase significantly due to growing interest in formic acid as a hydrogen carrier within the hydrogen economy.[12–15] Formic acid has a great potential as a hydrogen carrier due to being non-toxic, liquid at ambient conditions and its highly reversible nature, thus allowing for high purity H_2 through low/room temperature catalytic decomposition.[1,3,16,17]

The direct hydrogenation of carbon dioxide within the gaseous phase is thermodynamically unfavorable ($\Delta G^0 = 32.8$ kJ mol^{-1}).[18,19] Performing this reaction within the liquid phase through the usage of solvents results in a more favorable, exergonic reaction.[18–20] Additionally, the equilibrium of the reaction can be shifted towards the product side through the addition of bases, with particular interest in amines.[20] Commonly, nitrogen-containing bases such as trialkylamines are employed, resulting in the formation of adducts that strongly bind to the produced formic acid.[19,20] Previous work by Schaub *et al.* demonstrated the selection of the tertiary amine to be vital to allow for the desired reaction to occur, with a minimal protonation enthalpy of 50 kJ mol^{-1} being required to allow for formic acid production. Experimental studies by de Leeuw den Bouter *et al.* demonstrated similar behavior, with smaller, more reactive tertiary amines resulting in enhancement of CO_2 hydrogenation kinetics, while bulkier, less basic amines resulted in no to little formic acid formation.[43] The overall reaction equation including triethylamine (NEt_3) is given by:

$$H_2 + CO_2 + NEt_3 \rightleftharpoons [HNEt_3^+][HCOO^-] \qquad (1)$$

Previous works[21] have shown that the formic acid production rates scale directly with the amount of amine present, thus systems without a secondary solvent are desirable. Besides an increase in kinetic rates, the equilibrium is also further shifted towards formic acid at higher amine concentrations, therefore performing the reaction in pure trialkylamine systems without additional solvents would be highly attractive.

[a] Sustainable Process Engineering, Chemical Engineering and Chemistry, Eindhoven University of Technology, Eindhoven, The Netherlands.
E-mail: j.vanderschaaf@tue.nl
[b] Lab Hydrogen, ENGIE Lab CRIGEN, Stains, France
[c] Lab Biogas, Biomass and Waste, ENGIE Lab CRIGEN, Stains, France
† Electronic supplementary information (ESI) available. See DOI: https://doi.org/10.1039/d5cp00561b

However, previous works have shown that such formic acid – trialkylamine adducts are immiscible in non-binding trialkylamines until a critical molar ratio is achieved,[22] thus resulting in a possible biphasic system within the catalyst particles during formic acid production.

Several compositions of heterogeneous catalysts have been studied for the proposed reaction, based on a wide range of noble metals such as Au, Pt and Pd. While promising results were obtained for Pd-based and Pt-based catalysts at moderate temperatures and conditions, these catalysts often suffered from rapid deactivation and the production of significant amounts of undesired carbon monoxide.[1,17] Contrarily, extraordinary selectivity and stability has been previously demonstrated for gold supported catalysts, with no observable formation of undesired side-products and no catalyst deactivation.[21] Therefore, an Au/TiO$_2$ catalyst was selected within this work.

The objective of this study is to gain a deeper understanding into the implications of the biphasic nature of the amine – adduct system during the direct hydrogenation of CO_2 to formic acid. To this end, experiments were executed in batch reactors with and without the addition of additional solvents besides triethylamine. A 2D catalyst pore was modelled at mesoscale to allow for the study of intra-particle concentration profiles at a continuum level. The spinodal decomposition of the fluid mixture was modelled using phase field models following the Cahn–Hilliard equations coupled to the law of mass action with the diffuse interface approach.

2. Experimental materials and methods

2.1. Materials

Triethylamine ($>99.5\%$) was obtained from Sigma-Aldrich. Dibromomethane ($>99.9\%$, stabilized with butylhydroxytoluene) and 1,3,5-trimethoxybenzene ($>98.0\%$), were obtained from TCI chemicals. Acetonitrile-d_3 (D99.8%) and D_2O (D 99.0) were purchased from Deutero. 1-Decanol ($>98\%$) was purchased from Thermo Scientific Chemicals. All materials were used as received, handled in air and used without any additional purification. Commercial AUROlite Au/TiO$_2$ (1 wt% Au, verified with ICP-OES) was purchased from Strem. In order to prevent deactivation, the catalyst was stored under Ar in a cold and dark environment.

2.2. Analytical methods

^{1}H-NMR (Bruker, 400 MHz) was used to determine the chemical compositions of all samples from reactive experiments. Here, 0.5 mL of deuterated solvent (Acetonitrile-d_3 or D_2O) containing either dibromomethane or 1,3,5-trimethoxybenzene as internal standard was mixed with 0.1 mL of sample. The concentration of internal standard was 1 mol per liter.

Viscosity was measured using a Brookfield Devek DV2T Viscometer (61 spindle and 200 rpm). Densities were measured using a graduated cylinder 10 mL (±0.1 mL) and a Sartorius BP 211D scale.

2.3. Reactive testing

Reactive testing was conducted using a 270 mL fed – batch autoclave with integrated heating jacket at a constant working pressure of 15 bar. The temperature inside the reactor is monitored using a PT-100 thermal probe. In a typical experiment, 20 grams of AUROlite Au/TiO$_2$ was loaded into the reactor in air. The catalyst was received in the form of extrudates, and thus subsequently crushed and sieved to a particle size of 150–250 μm. Triethylamine (110 mL) was fed into the reactor, followed by flushing of the reactor with CO_2. H_2 and CO_2 are continuously fed using Bronkhorst mass flow controllers. A Bronkhorst back-pressure controller was used to ensure a constant pressure. Aliquots of the reaction mixture were obtained at every 10 hours. A 2 μm filter was present in the sample line to ensure no catalyst left the reactor. The reaction mixture was continuously stirred at 500 rpm.

3. Numerical methods

3.1. Phase field modelling

Phase field models enable the description of spontaneous phase separation of immiscible fluids.[23] Such models have previously been used to describe and simulate the grain growth of metal crystallites,[24] electromigration,[25] biological applications[26] and a simultaneous reversible chemical reaction with spinodal decomposition.[23,27]

Diffuse-interface phase field models are a versatile tool for microstructure simulations at mesoscale level.[28,29] Within this approach, the structures are described by a continuous set of phase-field variables, which are also continuous over the interface.[27] This way, the necessity of explicit front tracking is prevented, leading to decreased computational load.[28,29]

A commonly used example of such models is the Cahn–Hilliard equation. The Cahn–Hilliard equation describes the temporal evolution of spinodal decomposition through describing the Helmholtz free energy as a function of composition and the spatial derivative of the composition at the grid point.[30–33] Clavijo et al.[23] have previously presented a method to transform the Cahn–Hilliard equation into a thermodynamically consistent multicomponent reactive Cahn–Hilliard set of equations through the usage of n force balances and n mass balances to account for the chemical reactions. Here, n phase fields are considered in a set of coupled Cahn–Hilliard equations to represent the concentrations of all species (n), resulting in a system consisting of n nonlinear fourth order partial differential equations in space as a result of non-constant diffusion constants.

3.2. Governing equations and boundary conditions

An overview of the governing equations is given, further details on the derivation can be found elsewhere.[23,34]

Considering a n-species system where x_a, the mole fraction of component a, the sum of all mole fractions is given by

$$\sum_{a=1}^{n} x_a \equiv 1 \tag{2}$$

This journal is © the Owner Societies 2025

Phys. Chem. Chem. Phys., 2025, **27**, 19480–19487 | **19481**

and the gradient

$$\sum_{a=1}^{n} \nabla x_a \equiv 0 \tag{3}$$

From here it readily becomes apparent that the set is not linearly independent, thus we consider $n-1$ independent species, while the nth species is used as a reference to ensure mass conservation. The general balance consists of a diffusive flux ($\boldsymbol{J}^a$) and a reactive term (R^a)

$$\frac{\partial x_a}{\partial t} = -\nabla \cdot \boldsymbol{J}^a + R^a \tag{4}$$

The diffusive flux is given by

$$\boldsymbol{J}^a = -\sum_{b=1}^{n-1} L^{ab} \nabla \mu^b \tag{5}$$

with L_{ab} being the binary concentration-dependent diffusion coefficient and μ^b the chemical potential of component b.

$$L_{ab} = M_{ab} \varphi_a (\delta_{ab} - x_b) \tag{6}$$

Wherein M_{ab} are the binary diffusion coefficients, and δ_{ab} represents the Kronecker delta. The binary diffusion coefficients were determined by the Einstein–Stokes equation combined with the Stokes equation for low Reynold number flows:[35]

$$D_{ab} = \frac{k_B T}{6 \pi \eta r_a} \tag{7}$$

with T, η and r_a the temperature, the viscosity and molecular radius of component a respectively.

Per definition, the chemical potential of the system is equal to the variational derivative of free energy in respect to the species concentration and contains both the contribution of the n-well and interface contribution:

$$\mu_a = \left. \frac{\partial F}{\partial x_a} \right|_{P,V} \tag{8}$$

As was previously suggested by previous works,[23,30–33] the phase separation is assumed to be governed by the Ginzburg–Landau free energy ($\hat{\psi}$), expressed by

$$\hat{\psi}(x) = N_v k_B \vartheta \left(\sum_{a=1}^{n} x_a \ln x_a \right) + N_v \sum_{a=1}^{n} \sum_{b=1}^{n} \Omega^{ab} x_a x_b$$
$$+ \frac{1}{2} \sum_{a=1}^{n} \sum_{b=1}^{n} \Gamma^{ab} \nabla x_a \cdot \nabla x_b \tag{9}$$

where N_v, k_B and ϑ are the number of molecules of component a per unit volume, the Boltzmann constant and the temperature respectively. Ω^{ab} is the interaction energy between the mass fractions of components. Following previous works,[23,34] Ω^{ab} is defined by

$$\Omega^{ab} = 0 \text{ when } a = b \tag{10}$$

$$\Omega^{ab} = 2 k_B \vartheta_c^{ab} \text{ when } a \neq b \tag{11}$$

Here, ϑ_c^{ab} is the critical temperature between component a and b. Additionally, Γ^{ab} is the magnitude of the interfacial energy between components, with the unit of force:[30–33]

$$\Gamma^{ab} = \sigma^{ab} l^{ab} = N_v \Omega^{ab} (l^{ab})^2 \tag{12}$$

with σ^{ab} the interfacial tension and l^{ab} the interfacial thickness, as calculated by a 12–6 Lennard-Jones potential. The 12–6 potential was selected due to close agreement with experimental results for small molecules in solution[33]

$$l^{ab} = \left(\frac{11}{7} \right)^{\frac{1}{2}} \left(\frac{6}{\pi N_v} \right)^{\frac{1}{3}} \tag{13}$$

The expression for the chemical potential is given by

$$\mu_\sigma^a = N_v k_B T \ln \left(\frac{x_a}{x_\sigma} \right) + 2 N_v \sum_{b=1}^{n} (\Omega^{ab} - \Omega^{\sigma b}) x_b$$
$$- \sum_{b=1}^{n} (\Gamma^{ab} - \Gamma^{\sigma b}) \nabla \cdot (\nabla x_b) \tag{14}$$

Here, σ represents the σth conserved species and is used as a reference, following the work of Clavijo et al.[34]

Lastly, the reactive term (R^a) is based on the power law kinetics determined by Hensen et al.[21] for an Au/Al$_2$O$_3$ catalyst.

$$R_{\text{volumetric}} = k^+ \exp^{\frac{-E_a^+}{RT}} x_{CO_2} x_{H_2} \varphi_{\text{TEA}} - k^- \exp^{\frac{-E_a^-}{RT}} x_{\text{adduct}} \tag{15}$$

On the pore wall, distinctive active sites were placed, at which point the reactive term is added to the equations through a Dirichlet boundary condition. These active sites are modelled as a single bulk particle, meaning no distinction is made between different gold geometries within the active site. The volumetric kinetic expression presented in ref. 21 was rewritten to an intrinsic reaction rate per active site

$$R_{\text{intrinsic}} = R_{\text{volumetric}} \cdot \frac{\rho_{\text{site}} V_{\text{site}}}{\rho_{\text{solid}} \varepsilon_{\text{bed}} L_{\text{cat}}} \tag{16}$$

where ρ_{site} and ρ_{solid} are the gravimetric density of the active site and catalyst particle respectively. V_{site} is the volume of a single active site, ε_{bed} is the solid hold up within the reactor and L_{cat} is the active metal loading.

The dimensionless forms are introduced through a scaling based on a reference free energy ($\Psi_0 = 2 N_v k_B \vartheta$) as previously suggested.[34,36,37] The scaling is performed in order to improve numerical accuracy. This reference free energy is used to relate the free energy density to the species mobility

$$\boldsymbol{D}_{ab} = \Psi_0 M_{ab} x_a (\delta_{ab} - x_b) \tag{17}$$

Furthermore, the critical temperature and the length and time scales are scaled through[21,22]

$$\bar{y} = L_0^{-1} y \tag{18}$$

$$\bar{t} = T_0^{-1} t \text{ with } T_0 = \frac{D_0 l_0^2}{L_0^4} \tag{19}$$

$$\overline{\vartheta_c^{ab}} = T^{-1} \vartheta_c^{ab} \tag{20}$$

Here, D_0 and l_0 are set according to a reference species.

19482 | *Phys. Chem. Chem. Phys.*, 2025, **27**, 19480–19487

This journal is © the Owner Societies 2025

The reference species was taken to be the adduct. L_0 is set equal to the pore length. The resulting equations in dimensionless form are

$$\frac{\partial x_a}{\partial \bar{t}} = -\bar{\nabla} \cdot \overline{J_a} + \overline{R_a} \tag{21}$$

$$\overline{J_a} = -\sum_{b=1}^{n} \overline{\boldsymbol{D}_{ab}} \bar{\nabla} \bar{\mu}^b \tag{22}$$

$$\bar{\mu}_\sigma^b = \frac{1}{2} \ln \frac{x_b}{x_\sigma} + 2 \sum_{a=1}^{n} \left(\bar{\vartheta}_c^{ba} - \bar{\vartheta}_c^{\sigma a} \right) x_a$$
$$- \sum_{a=1}^{n} \left(\bar{\sigma}^{ba} \bar{\ell}^{ba} - \tilde{\sigma}^{\sigma a} \bar{\ell}^{\sigma a} \right) \nabla \cdot (\nabla x_a) \tag{23}$$

A zero flux (Neumann) boundary condition is enforced on the pore walls, except for the active metal sites. Here, the reaction term is implemented. The catalyst pore is assumed to be in contact with an external fluid reservoir, thus the continuity of fluxes between the solid and fluid phases in the form of a Dirichlet boundary condition is assumed. Initial concentrations are equal to saturation for all reagents.

3.3. Discretization

The mesoscale binodal decomposition simulations were performed in C++ using CVODE provided by SUNDIALS as a solver.[38,39]

Spatial discretization was performed using the finite volume method and the method of lines, while time discretization was performed by the CVODE solver. The time integration of Cahn–Hilliard equations is non-trivial due to the non-linear fourth order dependency in space as a result of non-constant, composition-dependent diffusion constants.[29,40] Thus, the adaptive-time step strategy was used. The maximum order of the BDF solver was set to 5, with a relative tolerance of 1×10^{-8}. Boundary conditions were discretized through second order Lagrange interpolation.

3.4. Physical properties

Adduct density and viscosity were experimentally determined as a function of temperature, and are depicted in the ESI† (S1 and S2) respectively. The Einstein–Stokes relation was used to calculate diffusivities, this relation requires the usage of molecular radii. An overview of the molecular radius of all components can be found in the ESI† (Table S1). The radius of the adduct was estimated based on the structure as proposed by Sprakel et al.[41] An overview of the resulting of resulting binary diffusion coefficients can be found in the ESI† (Table S2). The solubility of the gaseous reactants CO_2 and H_2 under the studied conditions was calculated using Henry's law. The Henry coefficients were determined at 50 degrees Celsius using the SRK property method in Aspen Plus V11, and are summarized in Table 1. The physical properties of the catalyst are given in Table 1.

Lastly, the studied process conditions are summarized in Table 2. In order to experimentally determine the critical temperature of the triethylamine adduct mixtures, a 1 : 1 molar ratio mixture was prepared and heated within a Rotavap. It was

Table 1 Overview of catalyst physical properties and Henry coefficients. Henry coefficients [mol m^{-3} bar^{-1}] for H_2 and CO_2 in triethylamine at 50 degrees Celsius. Coefficients were determined using the SRK property method in Aspen Plus V11

Parameter	Physical representation	Value	Unit	Source
$\rho_{Al_2O_3}$	Support density	4.01×10^3	kg$_{Al_2O_3}$ m$_{Al_2O_3}^{-3}$	42
ε_{bed}	Reactor solid hold-up	0.6	m$_{solid}^3$ m$_{reacter}^{-3}$	—
L_{cat}	Catalyst loading	0.01	kg$_{Au}$ kg$_{solid}^{-1}$	21
d_{site}	Active site diameter	1.9×10^{-9}	m	21
H_{CO_2}	Henry coefficient CO_2	40	mol m^{-3} bar	
H_{H_2}	Henry coefficient H_2	1.54	mol m^{-3} bar	

established that the mixture remains biphasic until all triethylamine has evaporated. For this reason, it was opted to set the critical temperature to the boiling point of triethylamine.

4. Results and discussion

Within this study, solventless batch experiments at elevated pressures were performed to gain insights into the performance of using triethylamine as an extraction base during the direct hydrogenation of CO_2 to formic acid. Afterwards, a 2D pore model describing spinodal decomposition was created in an attempt to further clarify the experimental results. Verification and validation of the model can be found in the ESI.†

4.1. Fed-batch experiments

First, the catalytic performance of a 1 wt% Au/TiO$_2$ catalyst in the direct hydrogenation of CO_2 at 15 bars of equimolar CO_2/H_2 mixture was tested using triethylamine as a base. In order to verify the activity of the received catalyst, an experiment was performed using a polar solvent to ensure solubility of all components. Here, a 1 : 3 vol/vol (0.45 mol mol^{-1}) mixture of triethylamine and 1-decanol was used, with the reaction a steady state formic acid concentration after 4 days, as shown in Fig. 1.

Next, with fresh catalyst an experiment was performed using pure neat triethylamine, without the addition of polar solvents. After 7 hours reaction time at otherwise identical conditions, the amount of FA observed in liquid samples was negligible. While exact determination of the concentrations was deemed inaccurate due to the very low concentrations, the estimated FA concentration is within the ppm range, whereas the experiment with solvent reached the thermodynamic equilibrium FA concentration expected based on the work of Hensen et al.[21]

In previous works, it was shown that such formic acid – triethylamine adducts are almost completely immiscible in neat triethylamine.[22] As FA is highly soluble in water, the spent

Table 2 Overview of simulation parameters

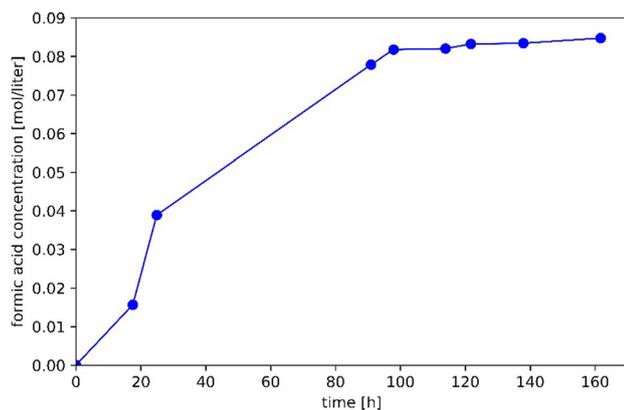| Parameter	Value	Unit
Temperature	323	K
Critical temperature	420	K
Pressure	15	bar
Relative tolerance	1×10^{-8}	—
Number of reactive sites	8	—
H_2 : CO_2 volumetric ratio	0.5	—

PCCP

Paper

Fig. 1 Concentration of FA in time. The reaction was run in a batch reactor. Total pressure 15 bar, temperature 50 °C, 1:3 vol/vol triethyl-amine: 1-decanol. H_2 and CO_2 feed was 5 min min^{-1} each.

catalyst was subsequently placed in 10 mL of demi water for 1 h after reaction. ^{1}H-NMR spectroscopy revealed a significant FA concentration, with the total molar amount of formic acid in the pores being approximately 3 orders of magnitude larger than those in the bulk fluid.

The verified catalyst activity and release of formic acid from the spent catalyst in the neat amine case, provide an initial indication that while formic acid is being produced, it cannot leave the pores. Even if the formation of formic acid in the form of formic acid – triethylamine adducts would result in phase separation with the reagents, the reaction would progress if the

product can diffuse away from the active site in order to retain low local concentrations. However, within the experiments, virtually no formic acid is observed to be present within the bulk fluid, providing an indication that the produced formic acid cannot diffuse away from the active site to reach the bulk liquid. This would result in high local concentrations of adduct within the pores of the catalyst resulting in a local equilibrium being reached around the active gold crystallites, therefore stopping the production of formic acid. To investigate this at pore level, a modelling approach is used.

4.2. Numerical modelling of catalyst pores

Numerical simulations were performed at meso-scale of a two-dimensional multicomponent system including spinodal decomposition representing the direct hydrogenation of CO_2 towards formic acid within a catalyst pore. Conditions were selected such to resemble the experimental protocol as closely as possible, with conditions summarized in Table 2.

The numerical simulations summarized in Table 2 were performed on a 40 × 40 cell grid, representing a physical size of 80 nm with the pore mouth exposed to a bulk liquid of constant concentration. The temporal evolution of the adduct front diffusing through the catalyst pore according to the process conditions summarized in Table 2 is shown in Fig. 2, while the temporal evolution of all species is shown in the ESI.†

Here, one distinctive active site was placed on the wall of the catalyst pore. It should be noted that the active sites are placed flat against the simulation boundaries, and thus do not occupy any volume. All simulations were started with the catalyst pore
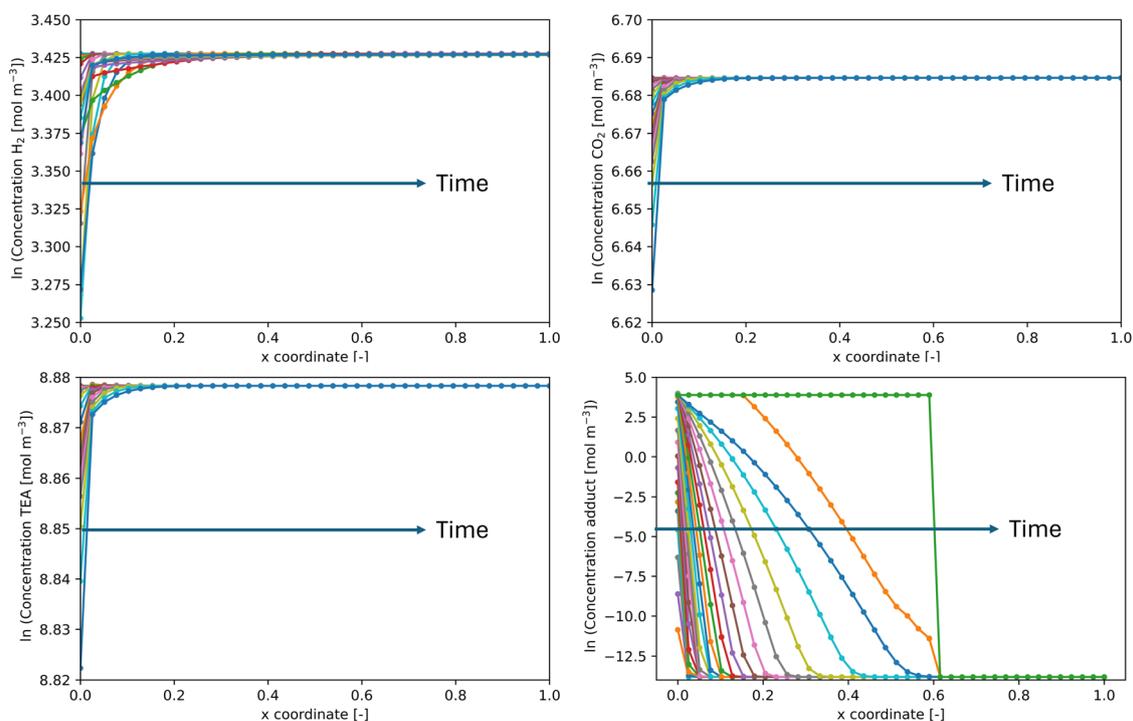

Fig. 2 Temporal evolution of FA formation over multiple active sites using a 40 × 40 cell grid, representing 80 × 80 nm. Simulation conditions can be found in Table 2 (temperature of 50 degrees Celsius, 15 bar total pressure).
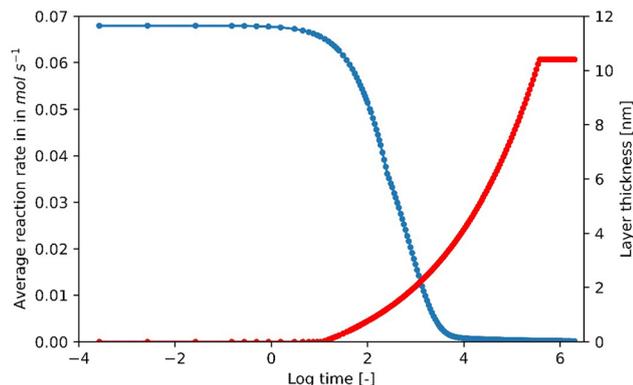
19484 | *Phys. Chem. Chem. Phys.*, 2025, **27**, 19480–19487

This journal is © the Owner Societies 2025

Fig. 3 Average adduct reaction rate and adduct layer thickness over a single active site. Simulation conditions can be found in Table 2 (temperature of 50 degrees Celsius, 15 bar total pressure).

filled with neat triethylamine, saturated with CO_2 and H_2. The initial adduct concentration was set to 1×10^{-6} mol m^{-3}.

Within Fig. 2, the formic acid concentration directly above the active site in the y-direction is visualized over time. Here, high concentrations of formic acid – triethylamine adducts of up to 48.6 mol m^{-3} are observed directly above the active site after approximately 10 seconds, while no formic acid is present within the bulk of the pore fluid. Then, the formic acid diffuses through the catalyst pore, forming a thin shell of adduct around the active site over a distance of several grid cells, thus showing the slight miscibility of the adduct and neat triethylamine, in line with previous experimental observations reported in ref. 22.

Fig. 3 depicts the average adduct reaction rate and the thickness of the adduct layer formed around a single gold crystallite. The thickness of the layer was determined directly on top of the active gold site, in the y-direction, with a grid cell being part of the adduct layer if the formic acid concentration is > 0.1 mol m^{-3}. Here, initially a high formic acid formation rate of 0.067 mol s^{-1} is observed, followed by a rapid decline until the production rate of formic acid is decreased to nearly zero (0.0002 mol s^{-1}). While the observed reaction rate is close to zero, Fig. 2 reveals that the reagents (CO_2, H_2 and triethylamine) are not depleted but present at the active site close to saturation concentrations.

Therefore, the net zero production rate is not caused by diffusion limitations or unavailability of the reagents at the active site, but by local equilibrium conditions being achieved around the active site, as evident from the equal forward and backward reaction rates, which are equal to ~ 0.008 mol s^{-1}.

As evident from Fig. 3, the thickness of the adduct layer follows an opposite trend to the adduct production rate, with the adduct concentration within the bulk fluid remaining equal to zero during the initial highly reactive period. After approximately 10 seconds, the decrease in formic acid production rates corresponds with the moment the formed adduct starts to diffuse away from the active site to form a layer around the active site, with the layer thickness growing up to 10.6 nm. The slow diffusion rate of the product away from the active site is

also evident from the diffusivity of the adduct within the neat amine phase, which is found to be equal to 6.63×10^{-12}, compared to $\sim 8.49 \times 10^{-9}$ for the gaseous reagents within the neat amine phase. Thus, the inability of the product to diffuse away from the active sites results in a local equilibrium condition forming around the active site, thereby reducing the average reaction rate to zero.

Simulations were also performed for larger catalyst pores. The temporal evolution of a larger catalyst pore is shown in the ESI† (Fig. S8). Upon expending the pore size to 200 nm and placing 4 evenly spaced active sites on each side of the catalyst pore, the trends observed for the single active site are also observed for the larger pore. Here, despite a larger adduct productivity capacity due to the presence of multiple active sites, only a thin layer of adduct is formed around the active sites before reducing the average reaction rate to nearly zero due to the inability of the product to diffuse towards the bulk phase and therefore locally reaching the equilibrium condition. These numerical observations show comparable behavior to the experimental observations, in which formic acid was observed to be present within the catalyst pores, but not in the bulk reaction fluid.

5. Conclusion

Solventless batch experiments at elevated pressures were performed to gain insights into the performance of using triethylamine as an extraction base during the direct hydrogenation of CO_2 to formic acid.

After several hours of reaction, no formic acid was observed within the bulk liquid of the batch experiments. Due to the biphasic nature of formic acid – triethylamine systems, the formic acid concentration within the catalyst pores after reaction was evaluated by placing the spent catalyst in water. Here, the total molar amount of formic acid in the pores being orders of magnitude larger than those in the reactor fluid.

In order to investigate this at pore level, a 2D model describing spinodal decomposition was created and verified in C++. Here, the Cahn–Hilliard equation was used to describe the temporal evolution of spinodal decomposition through describing the Helmholtz free energy as a function of composition and the spatial derivative of the composition at the grid point.

The biphasic nature of the tertiary alkylamine – formic acid system was found to have significant implications for the reaction performance of the proposed system. The inability of the adduct to dissolve in the available non-binding amine results in the catalyst pores readily reaching the equilibrium condition, therefore reducing the average reaction rate by two orders of magnitude, from 0.067 to 0.0002 mol s^{-1}.

These results highlight the need for an secondary polar solvent such as 1-decanol to allow for formic acid production to enable formic acid – tertiary amine solubility, for *e.g.* hydrogen storage applications. As the usage of such solvents was demonstrated to be inevitable when performing the reaction

This journal is © the Owner Societies 2025

Phys. Chem. Chem. Phys., 2025, **27**, 19480–19487 | **19485**

with tertiary amines, future works should focus on the optimalization of the solvent-amine combination to further develop the proposed process.

Conflicts of interest

There are no conflicts to declare.

Data availability

Data and code will be made available upon reasonable request to the corresponding author.

Acknowledgements

References

1 R. Sun, et al., Heterogeneous catalysts for CO_2 hydrogenation to formic acid/formate: From nanoscale to single atom, Energy Environ. Sci., 2021, 14(3), 1247–1285, DOI: 10.1039/d0ee03575k.

2 M. Cokoja, C. Bruckmeier, B. Rieger, W. A. Herrmann and F. E. Kühn, Transformation of carbon dioxide with homogeneous transition-metal catalysts: A molecular solution to a global challenge?, Angew. Chem., Int. Ed., 2011, 50(37), 8510–8537, DOI: 10.1002/anie.201102010.

3 S. Kushwaha, J. Parthiban and S. K. Singh, Recent Developments in Reversible CO2 Hydrogenation and Formic Acid Dehydrogenation over Molecular Catalysts, ACS Omega, 2023, 8(42), 38773–38793, DOI: 10.1021/acsomega.3c05286.

4 J. Vansant, Carbon Dioxide Emission and Merchant Market in the European Union, 2003.

5 IPCC, 1.5 °C Global Warming CH4: Strengthening and Implementing the Global Response, 2022.

6 Intergovernmental Panel on Climate Change, Climate Change 2022: Mitigation of Climate Change Technical Summary, 2022.

7 S. Moret, P. J. Dyson and G. Laurenczy, Direct synthesis of formic acid from carbon dioxide by hydrogenation in acidic media, Nat. Commun., 2014, 5, 1–7, DOI: 10.1038/ncomms5017.

8 M. Scott, B. Blas Molinos, C. Westhues, G. Franciò and W. Leitner, Aqueous Biphasic Systems for the Synthesis of Formates by Catalytic CO2 Hydrogenation: Integrated Reaction and Catalyst Separation for CO2-Scrubbing Solutions, ChemSusChem, 2017, 10(6), 1085–1093, DOI: 10.1002/cssc.201601814.

9 A. Rosas-Hernández, C. Steinlechner, H. Junge and M. Beller, Chemical Transformations of Carbon Dioxide, 2017.

10 C. Kim, et al., Accelerating the net-zero economy with CO2-hydrogenated formic acid production: Process development and pilot plant demonstration, Joule, 2024, 8(3), 693–713, DOI: 10.1016/j.joule.2024.01.003.

11 M. Pérez-Fortes, J. C. Schöneberger, A. Boulamanti, G. Harrison and E. Tzimas, Formic acid synthesis using CO2 as raw material: Techno-economic and environmental evaluation and market potential, Int. J. Hydrogen Energy, 2016, 41(37), 16444–16462, DOI: 10.1016/j.ijhydene.2016.05.199.

12 M. Byun, A. Lee, S. Cheon, H. Kim and H. Lim, Preliminary feasibility study for hydrogen storage using several promising liquid organic hydrogen carriers: Technical, economic, and environmental perspectives, Energy Convers. Manag., 2022, 268, 116001, DOI: 10.1016/j.enconman.2022.116001.

13 D. D. Papadias, J. K. Peng and R. K. Ahluwalia, Hydrogen carriers: Production, transmission, decomposition, and storage, Int. J. Hydrogen Energy, 2021, 46(47), 24169–24189, DOI: 10.1016/j.ijhydene.2021.05.002.

14 J. Eppinger and K. W. Huang, Formic Acid as a Hydrogen Energy Carrier, ACS Energy Lett., 2017, 2(1), 188–195, DOI: 10.1021/acsenergylett.6b00574.

15 J. O. M. Bockris, The hydrogen economy: Its history, Int. J. Hydrogen Energy, 2013, 38(6), 2579–2588, DOI: 10.1016/j.ijhydene.2012.12.026.

16 G. H. Gunasekar, K. Park, K. D. Jung and S. Yoon, Recent developments in the catalytic hydrogenation of CO2 to formic acid/formate using heterogeneous catalysts, Inorg. Chem. Front., 2016, 3(7), 882–895, DOI: 10.1039/c5qi00231a.

17 A. Álvarez, et al., Challenges in the Greener Production of Formates/Formic Acid, Methanol, and DME by Heterogeneously Catalyzed CO2 Hydrogenation Processes, Chem. Rev., 2017, 117(14), 9804–9838, DOI: 10.1021/acs.chemrev.6b00816.

18 R. Tanaka, M. Yamashita, L. W. Chung, K. Morokuma and K. Nozaki, Mechanistic studies on the reversible hydrogenation of carbon dioxide catalyzed by an Ir-PNP complex, Organometallics, 2011, 30(24), 6742–6750, DOI: 10.1021/om2010172.

19 T. Schaub and R. A. Paciello, A process for the synthesis of formic acid by CO2 hydrogenation: Thermodynamic aspects and the role of CO, Angew. Chem., Int. Ed., 2011, 50(32), 7278–7282, DOI: 10.1002/anie.201101292.

20 D. Preti, C. Resta, S. Squarcialupi and G. Fachinetti, Carbon dioxide hydrogenation to formic acid by using a heterogeneous gold catalyst, Angew. Chem., Int. Ed., 2011, 50(52), 12551–12554, DOI: 10.1002/anie.201105481.

21 G. A. Filonenko, W. L. Vrijburg, E. J. M. Hensen and E. A. Pidko, On the activity of supported Au catalysts in the liquid phase hydrogenation of CO2 to formates, J. Catal., 2016, 343, 97–105, DOI: 10.1016/j.jcat.2015.10.002.

22 A. W. N. de Leeuw den Bouter, E. J. M. Vogels, A. Miquelot, L. Brito, P. Olivier and J. van der Schaaf, Chemical and Phase Equilibrium of Formic Acid-Trialkylamine Complexes, ACS Omega, 2025, 10, 27735–27744, DOI: 10.1021/acsomega.4c10897.

23 S. P. Clavijo, A. F. Sarmiento, L. F. R. Espath, L. Dalcin, A. M. A. Cortes and V. M. Calo, Reactive [n]-species Cahn–Hilliard system: A thermodynamically-consistent model for reversible chemical reactions, J. Comput. Appl. Math., 2019, 350, 143–154, DOI: 10.1016/j.cam.2018.10.007.

24 M. Honjo and Y. Saito, Numerical simulation of phase separation in Fe-Cr binary and Fe-Cr-Mo ternary alloys with use of the Cahn-Hilliard equation, *ISIJ Int.*, 2000, **40**(9), 914–919, DOI: **10.2355/isijinternational.40.914**.

25 D. N. Bhate, A. Kumar and A. F. Bower, Diffuse interface model for electromigration and stress voiding, *J. Appl. Phys.*, 2000, **87**(4), 1712–1721, DOI: **10.1063/1.372082**.

26 Q. Du, C. Liu and X. Wang, Simulating the deformation of vesicle membranes under elastic bending energy in three dimensions, *J. Comput. Phys.*, 2006, **212**(2), 757–777, DOI: **10.1016/j.jcp.2005.07.020**.

27 J. J. Christensen, K. Elder and H. C. Fogedby, Phase segregation dynamics of a chemically reactive binary mixture, *Phys. Rev. E*, 1996, **54**(3), 2212–2215, DOI: **10.1103/PhysRevE.54.R2212**.

28 N. Moelans, B. Blanpain and P. Wollants, An introduction to phase-field modeling of microstructure evolution, *CALPHAD: Comput. Coupling Phase Diagrams Thermochem.*, 2008, **32**(2), 268–294, DOI: **10.1016/j.calphad.2007.11.003**.

29 H. Gómez, V. M. Calo, Y. Bazilevs and T. J. R. Hughes, Isogeometric analysis of the Cahn-Hilliard phase-field model, *Comput. Methods Appl. Mech. Eng.*, 2008, **197**(49–50), 4333–4352, DOI: **10.1016/j.cma.2008.05.003**.

30 J. W. Cahn, Phase separation by spinodal decomposition in isotropic systems, *J. Chem. Phys.*, 1965, **42**(1), 93–99, DOI: **10.1063/1.1695731**.

31 J. W. Cahn and J. E. Hilliard, Free energy of a nonuniform system. III. Nucleation in a two-component incompressible fluid, *J. Chem. Phys.*, 1959, **31**(3), 688–699, DOI: **10.1063/1.1730447**.

32 J. W. Cahn, Free energy of a nonuniform system. II. Thermodynamic basis, *J. Chem. Phys.*, 1959, **30**(5), 1121–1124, DOI: **10.1063/1.1730145**.

33 J. W. Cahn and J. E. Hilliard, Free energy of a nonuniform system. I. Interfacial free energy, *J. Chem. Phys.*, 1958, **28**(2), 258–267, DOI: **10.1063/1.1744102**.

34 S. P. Clavijo, L. Espath and V. M. Calo, Extended Larché–Cahn framework for reactive Cahn–Hilliard multicomponent systems, *Continuum Mech. Thermodyn.*, 2021, **33**(6), 2391–2410, DOI: **10.1007/s00161-021-01045-9**.

35 P. Atkins, *Physical chemistry*, 10th edn, 2017.

36 V. Blickle, T. Speck, C. Lutz, U. Seifert and C. Bechinger, Einstein relation generalized to nonequilibrium, *Phys. Rev. Lett.*, 2007, **98**(21), 1–4, DOI: **10.1103/PhysRevLett.98.210601**.

37 A. Einstein, Über die von der molekularkinetischen Theorie der Wärme geforderte Bewegung von in ruhenden Flüssigkeiten suspendierten Teilchen, *Ann. Phys.*, 1905, **322**(8), 549–560, DOI: **10.1002/andp.19053220806**.

38 A. C. Hindmarsh, *et al.*, SUNDIALS: Suite of nonlinear and differential/algebraic equation solvers, *ACM Trans. Math. Softw.*, 2005, **31**(3), 363–396, DOI: **10.1145/1089014.1089020**.

39 D. J. Gardner, D. R. Reynolds, C. S. Woodward and C. J. Balos, Enabling New Flexibility in the SUNDIALS Suite of Nonlinear and Differential/Algebraic Equation Solvers, *ACM Trans. Math. Softw.*, 2022, **48**(3), 31, DOI: **10.1145/3539801**.

40 J. Kim, K. Kang and J. Lowengrub, Conservative Multigrid Methods for Ternary Cahn-Hilliard Systems, *Commun. Math. Sci.*, 2004, **2**(1), 53–77, DOI: **10.4310/CMS.2004.v2.n1.a4**.

41 L. M. J. Sprakel and B. Schuur, Solvent developments for liquid-liquid extraction of carboxylic acids in perspective, *Sep. Purif. Technol.*, 2019, **211**, 935–957, DOI: **10.1016/j.seppur.2018.10.023**.

42 NIST center for neuron research, Reference tables. **https://www.nist.gov/ncnr/sample-environment/sample-mounting/reference-tables** (accessed Apr. 05, 2024).

43 A. W. N. De Leeuw Den Bouter, L. M. Meijer, L. Brito, A. Miquelot, P. Olivier and J. Van Der Schaaf, Effect of Tertiary Amine Selection on CO2 to Formic Acid Hydrogenation with the Au-np Catalyst, *Ind. Eng. Chem. Res.*, 2025, **64**, 8109–8118, DOI: **10.1021/acs.iecr.4c04902**.

This journal is © the Owner Societies 2025

Phys. Chem. Chem. Phys., 2025, **27**, 19480–19487 | **19487**